

See discussions, stats, and author profiles for this publication at: <https://www.researchgate.net/publication/271704978>

Polymorph Selection and Structure Evolution of CaCO_3 Mesocrystals under Control of Poly(sodium 4-styrenesulfonate): Synergetic Effect of Temperature and Mixed Solvent

ARTICLE in CRYSTAL GROWTH & DESIGN · OCTOBER 2014

Impact Factor: 4.89 · DOI: 10.1021/cg5012132

CITATIONS

6

READS

30

3 AUTHORS, INCLUDING:



Lei Liu

University of Science and Technology of China

12 PUBLICATIONS 289 CITATIONS

SEE PROFILE



Shu-Hong Yu

University of Science and Technology of China

368 PUBLICATIONS 15,666 CITATIONS

SEE PROFILE

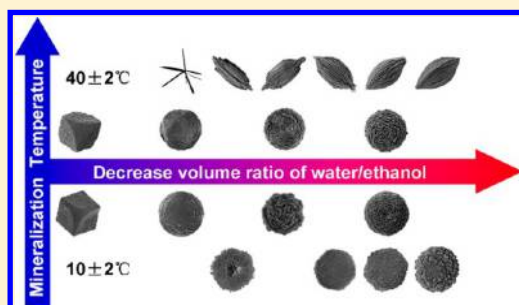
Polymorph Selection and Structure Evolution of CaCO_3 Mesocrystals under Control of Poly(sodium 4-styrenesulfonate): Synergetic Effect of Temperature and Mixed Solvent

Lei Liu, Jun Jiang, and Shu-Hong Yu*

Division of Nanomaterials and Chemistry, Hefei National Laboratory for Physical Sciences at Microscale, Collaborative Innovative Center of Suzhou Nano Science and Technology, Department of Chemistry, University of Science and Technology of China, Hefei 230026, P. R. China

S Supporting Information

ABSTRACT: The synergetic effects of water/ethanol mixed solvent and crystallization temperature upon CaCO_3 polymorph discrimination and structural assembly under control of poly(sodium 4-styrenesulfonate) (PSS) were examined. CaCO_3 mesocrystals of all three anhydrous polymorphs (calcite, aragonite, and vaterite) with progressively developed morphologies can be selectively realized in one system by consecutively decreasing the water/ethanol volume ratio (R) at the proper temperature. At a lower crystallization temperature ($10\text{ }^\circ\text{C}$), decreasing the R value resulted in a polymorph transition of CaCO_3 from pure calcite to pure vaterite, which was mainly attributed to the increased ethanol content and the resulting conformation change of PSS molecules. In contrast, CaCO_3 polymorphs changed from pure calcite to almost pure aragonite at higher crystallization temperature ($40\text{ }^\circ\text{C}$), where the temperature effect was more obvious and became the dominant parameter for CaCO_3 polymorph selection. In addition, a dipole effect was employed to explain the formation of calcite and vaterite mesocrystals with continuously and increasingly developed superstructures. This study could have important implications in the design and preparation of a great deal of inorganic materials with well-defined morphologies, polymorphs, and ordered arrangement that can be controlled by simply adjusting the reaction media and temperature.



1. INTRODUCTION

Living organisms can exert highly accurate control over size, morphology, polymorph, and orientation of inorganic minerals and arrange them into highly ordered and hierarchically organized structures from nanoscale to macroscale^{1,2} for specific purposes, such as structural support,³ protection,⁴ navigation,⁵ and photosensitivity.⁶ Mollusk shell, renowned for its superior mechanical properties, is an excellent example, in which the outer prismatic layer is composed of an organization of large calcite single-crystal prisms, whereas the inner nacreous layer is assembled by aragonite platelets with a brick-and-mortar architecture.⁷ Inspired by the formation process of biominerals occurring in nature, artificial mineralization using bioinspired techniques and formation mechanisms has received considerable attention and remains a hot research topic, as recently reviewed.^{8–10}

Calcium carbonate (CaCO_3) is one of the most studied subjects in bioinspired mineralization because of its abundant existence in the biosphere and lithosphere¹¹ and its wide industrial applications, for example, as filler in paint, rubber, and paper.¹² Furthermore, it can also be used as a precursor¹³ or a new template^{14,15} to prepare various mesoporous materials, such as calcium phosphate and silica. CaCO_3 mesocrystals could be further employed as novel carriers for drug delivery due to their high porosity, biocompatibility, and biodegrad-

ability, as we previously reported.¹⁶ Several kinds of soft and hard templates, including biopolymers,^{17–19} double hydrophilic block copolymers (DHBCs),^{20,21} self-assembled monolayers,²² biogenic systems,^{23,24} colloidal particle assemblies,^{25,26} and polymer networks,^{27,28} have been chosen to direct and mediate CaCO_3 crystallization. A great deal of subtle CaCO_3 (super)-structures have been realized, such as pancakes,²⁹ mono-dispersed spheres,³⁰ fibers,^{31,32} layered structures,^{33–35} mesocrystals,^{36,37} and complex single crystals.^{25,38} Moreover, polymorph discrimination of CaCO_3 minerals, which usually involves altering the crystallization temperature,³⁹ solvent media composition,^{30,40} and concentration of Ca^{2+} and/or additives,^{41–43} is another long-standing challenge that is attracting increasing attention for its important role in biomineralization as it occurs in mollusk shell.⁷ Therefore, precise control over the polymorph, morphology, and orientation of CaCO_3 in one system is of great interest from the viewpoints of both scientific research and practical applications.

Various reaction conditions, such as concentrations of reactants and additives, temperature, and solvent nature, can

Received: August 16, 2014

Revised: October 9, 2014

Published: October 13, 2014

have significant influences upon the crystallization of inorganic crystals. Therefore, the polymorph and morphology of CaCO_3 minerals are directed by both thermodynamic and kinetic factors.⁴⁴ Generally speaking, kinetic driving systems can lead to remarkable deviations in the growth habit of CaCO_3 from thermodynamic models. In particular, it should be mentioned that kinetic factors such as solvent nature and reaction temperature play crucial roles in mediating the crystallization behavior and polymorph selection of CaCO_3 . An amorphous calcium carbonate (ACC) film can be produced on a matrix surface modified with $-\text{OH}$ groups at a relatively low temperature of 4°C .⁴⁵ However, in the presence of poly(acrylic acid) (PAA), calcite fibers were obtained via a solution–precursor–solid mechanism at the same temperature (4°C).³¹ Spherical vaterite aggregates were synthesized at 50°C .⁴⁶ In addition, crystallization in mixed solvents is emerging and has been proved to be a new way toward fabrication of hierarchical superstructures.^{47–49} The addition of simple alcohols into the aqueous medium for CaCO_3 mineral growth can induce the formation of hopper crystals via redressing the thermodynamic–kinetic balance.⁴⁴ By varying the reaction temperature and solvent composition simultaneously, complex vaterite with multilayered structure and aragonite rods can be selectively formed at relative high temperatures (ca. 90 – 120°C) in water/ethanol mixtures.⁵⁰ However, the synergistic effects of reaction temperature and solvent nature in the presence of polyelectrolyte additives on the crystallization habits of CaCO_3 have not been systematically studied, despite a few previous reports. Thus, this topic remains a challenge that needs further extensive exploration.

In a recent paper, we presented a simple water/ethanol system in which CaCO_3 mesocrystals and superstructures could be prepared with progressively evolving stages under thermodynamic–kinetic control that resulted from altering the water/ethanol volume ratio at room temperature.⁵¹ However, only two polymorphs (calcite and vaterite) could be selectively obtained, and we could not even get pure vaterite. Therefore, we aim to introduce another kinetic parameter, reaction temperature, to investigate the crystallization process of CaCO_3 in more detail and, we expect, with more variations. A slightly higher Ca^{2+} concentration and a lower polymer concentration were adopted here to reduce their mediation over CaCO_3 crystallization, and thus relatively increase the influences of other parameters, such as solvent nature and temperature, which is intuitively obvious. In the present study, we will demonstrate that the polymorph selection of all three anhydrous CaCO_3 phases (calcite, aragonite, and vaterite) with (almost) pure composition and uniform mesoscale-assembled nanoparticle superstructures (so-called mesocrystals) can be well manipulated simply by adjusting reaction temperature and solvent media composition with constant additive concentration, which has been rarely reported in one crystallization system until now.

2. EXPERIMENTAL SECTION

2.1. Chemicals. Analytical-grade chemical reagents bought from manufacturers were used directly for CaCO_3 crystallization without any further purification treatment. Poly(sodium 4-styrenesulfonate) (PSS, $M_w = 70\,000\text{ g}\cdot\text{mol}^{-1}$) was purchased from Fluka. Both calcium chloride (CaCl_2 , $M_w = 110.98\text{ g}\cdot\text{mol}^{-1}$) and ammonium bicarbonate (NH_4HCO_3 , $M_w = 79.06\text{ g}\cdot\text{mol}^{-1}$) were purchased from Sinopharm Chemical Reagent Co., Ltd.

2.2. Synthetic Procedures. All glassware, including glass bottles ($25 \times 40\text{ mm}$) and glass slices ($5 \times 5 \times 1\text{ mm}$), was treated as

following to make them hydrophilic. First, they were successively washed with ethanol and deionized water (DIW , $18.2\text{ M}\Omega\cdot\text{cm}^{-1}$) under sonification to remove any adsorbate on their surface. Then, they were treated with piranha solution ($\text{H}_2\text{SO}_4/\text{H}_2\text{O}_2$ mixture with a volume ratio of 7/3) at about 90°C . After a 2-day treatment, they were adequately washed with DIW and finally dried with acetone.

A slow gas–liquid diffusion process was employed to synthesize CaCO_3 crystals as we previously reported⁵¹ (see Supporting Information, Figure S1). In a typical synthesis, CaCl_2 (1.5 mM) and PSS ($0.5\text{ g}\cdot\text{L}^{-1}$) were dissolved into DIW or DIW/ethanol mixtures with different volume ratios (R) under magnetic stirring in several glass bottles (red color in Figure S1). Then several glass slices (blue color in Figure S1), acting as substrate to collect CaCO_3 crystals, were put into each glass bottle. Subsequently, a piece of Parafilm (green color in Figure S1) with three punched needle holes was used to cover each glass bottle, placed in a closed desiccator. Meanwhile, a few other small glass bottles (10 mL) filled with crushed NH_4HCO_3 (purple color in Figure S1) were also sealed by Parafilm with three punched needle holes and placed at the bottom of the desiccator. Finally, the desiccator was moved into an incubator to keep the reaction temperature constant during the whole crystallization process. The mineralization reaction was carried out at two different temperatures, 10 ± 2 and $40 \pm 2^\circ\text{C}$. After a certain period of crystallization time, the glass slices were taken out from the reaction solutions, washed several times with DIW and ethanol respectively, and finally dried under ambient conditions for further characterization.

2.3. Characterization. The dried CaCO_3 samples were characterized by powder X-ray diffraction (XRD), scanning electron microscopy (SEM), transmission electron microscopy (TEM), high-resolution TEM (HR-TEM), and selected area electron diffraction (SAED). The XRD analysis was performed on an MXP 18 AHF X-ray diffractometer (MAC Science Co. Ltd.) using the monochromatized wavelength (λ) of 1.54056 \AA from $\text{Cu K}\alpha$ radiation as the radioactive source. After the dry samples were sputtered with a thin layer of gold, SEM images were obtained from a SUPRA 40 field emission scanning electron microscope (Zeiss) operating at 5 kV accelerating voltage. TEM and HR-TEM images and corresponding SAED patterns were recorded on an H-800 model transmission electron microscope (Hitachi) working under 200 kV accelerating voltage.

3. RESULTS AND DISCUSSION

3.1. Crystallization of CaCO_3 Mesocrystals at $10 \pm 2^\circ\text{C}$. The modifications on the polymorph of as-prepared CaCO_3 crystals with different R values at $10 \pm 2^\circ\text{C}$ in the presence of PSS were examined by XRD analysis (Figure 1). It was easily found that low ethanol content in mixed solvents (i.e., $R = 10/0$ and $R = 8/2$) resulted in the formation of pure calcite (JCPDS card no. 05-0568), as shown in Figure 1a,b. However, the

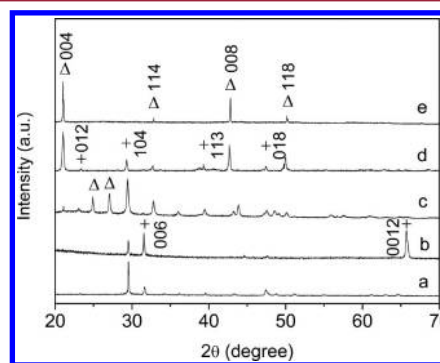


Figure 1. XRD patterns of the CaCO_3 samples obtained after 24 h crystallization at $10 \pm 2^\circ\text{C}$ with different R values: 10/0 (a); 8/2 (b); 6/4 (c); 5/5 (d); 3/7 (e). The concentrations of Ca^{2+} and PSS were 1.5 mM and $0.5\text{ g}\cdot\text{L}^{-1}$, respectively. + and Δ here indicate peaks for calcite and vaterite, respectively.

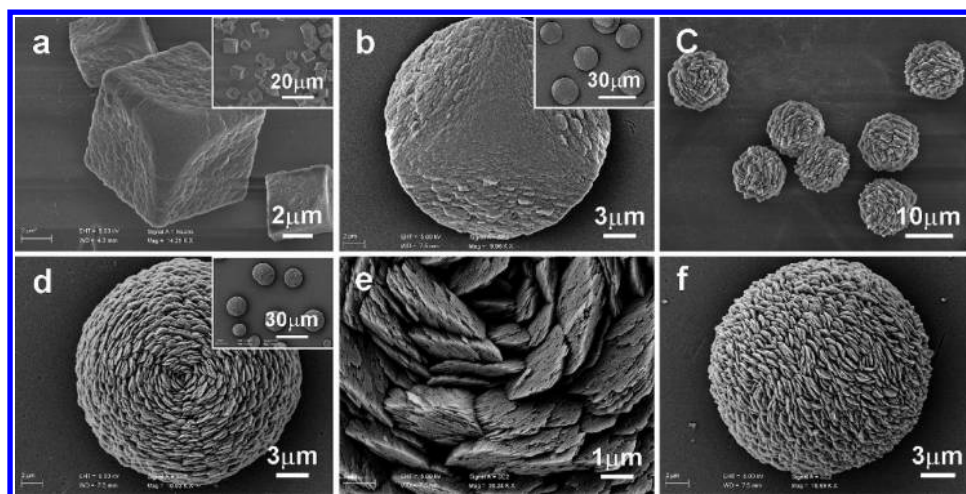


Figure 2. SEM images of calcite mesocrystals obtained after 24 h crystallization at 10 ± 2 °C with different R values: 10/0 (a); 8/2 (b); 6/4 (c); 5/5 (d–f). Insets in panels (a), (b), and (d) display the low-magnification overview of calcite mesocrystals. Panels (e) and (f) are enlarged and side views of the sample displayed in (d). The concentrations of Ca^{2+} and PSS were 1.5 mM and $0.5 \text{ g}\cdot\text{L}^{-1}$, respectively.

CaCO_3 sample obtained with an R value of 6/4 can be indexed as a mixture of calcite and vaterite (JCPDS card no. 33-0268) (Figure 1c), where calcite was dominant. When the R value was decreased to 5/5, vaterite became the dominant phase in the mixture (Figure 1d). All the above variations in the CaCO_3 polymorphs are similar to those observed in our previous report.⁵¹ However, pure vaterite can be obtained at the smallest R value of DIW/ethanol ($R = 3/7$), as indexed in Figure 1e, in contrast to what occurred at room temperature, where we could not synthesize pure vaterite.⁵¹ The change of CaCO_3 polymorphs from pure calcite to mixtures of calcite and vaterite, and finally to pure vaterite, can be selectively realized by choosing the proper R value of DIW/ethanol at a relatively low crystallization temperature (10 ± 2 °C), as reflected in the XRD patterns (Figure 1). The sharp and strong diffraction peaks of the (001) faces for both calcite (Figure 1b) and vaterite (Figure 1d,e) can be attributed to the large-area exposure of these faces, which can be clearly observed from their SEM images, shown in later discussions.

Typical SEM images of calcite mesocrystals prepared at different R values with PSS present ($0.5 \text{ g}\cdot\text{L}^{-1}$) after 24 h crystallization at 10 ± 2 °C are displayed in Figure 2. It can be clearly observed that increasing the ethanol content in solvent mixtures can dramatically influence the growth and phase development of calcite mesocrystals. Truncated calcite rhombohedrons with a size range of $5.6\text{--}12.5 \mu\text{m}$ can be obtained in aqueous solution (Figure 2a). Though the exposure of the (001) face is obvious, these rhombohedrons are mostly bounded by (104) faces, which suggests that the influence of PSS is weak in the aqueous system in the present case. Besides, there also appears a finer texture of the primary building blocks on the (104) faces, as shown in Figure 2a. Monodisperse calcite mesoscale assemblies with rounded shape are observed at $R = 8/2$ (Figure 2b). Both the exposure of the (001) face and the layered structures on the (104) faces are more pronounced. The size in the direction of the c axis is shortened apparently, indicating that the efficiency of aggregation of primary building blocks is lowered along the c axis of calcite. Further increasing ethanol concentration results in a totally different but related spherical morphology, as shown in Figure 2c–f. The whole structure (Figure 2c,d) and its building blocks, further stacked by several nanosheets (Figure 2e), are very porous. By

decreasing the R value of DIW/ethanol in the mixed solvent, the growth and development stages of calcite mesocrystals mainly undergo a “truncated rhombohedron–rounded multilayered structure–sphere” transformation process. What is more, it should be mentioned that the addition of ethanol leads to calcite mesocrystals that are quite homogeneous in size and morphology (Figure 2b–d).

The structure of a single platelet unit making up these multilayered calcite mesocrystals is further analyzed in detail using TEM, HR-TEM, and SAED (Figure 3). The SAED

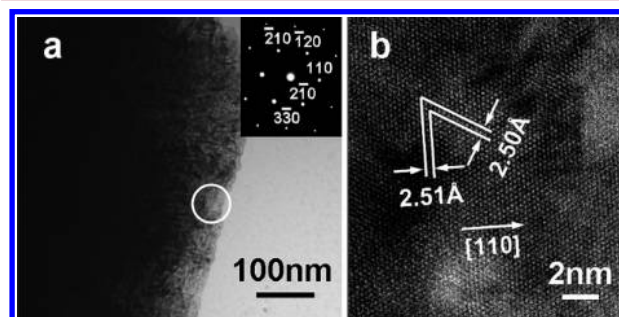


Figure 3. Representative TEM (a) and HR-TEM (b) images of the multilayered CaCO_3 samples obtained after 24 h crystallization at 10 ± 2 °C with R value of 8/2. Inset in panel (a) corresponds to the SAED pattern taken along calcite [001]. The concentrations of Ca^{2+} and PSS were 1.5 mM and $0.5 \text{ g}\cdot\text{L}^{-1}$, respectively.

pattern, indexed as a calcite crystal viewed from the [001] zone axis, confirms its single-crystal nature. This in turn verifies that the most exposed planes of the platelets are the (001) planes of calcite, as indexed in its XRD pattern (Figure 1b). The lattice distances in the HR-TEM image, with measured values of 2.51 and 2.50 Å (Figure 3b), agree very well with calcite {110} lattice spacing found in standard XRD data (2.495 Å, JCPDS card no. 05-0586). Clearly, there also exists an amorphous phase (ACC) or some defects which could be reflected from the light area with low contrast in the HR-TEM image (Figure 3b).

As we reported previously,⁵¹ the addition of ethanol into a Ca-PSS aqueous system induces the formation of a metastable polymorph of CaCO_3 (vaterite). However, significant variations

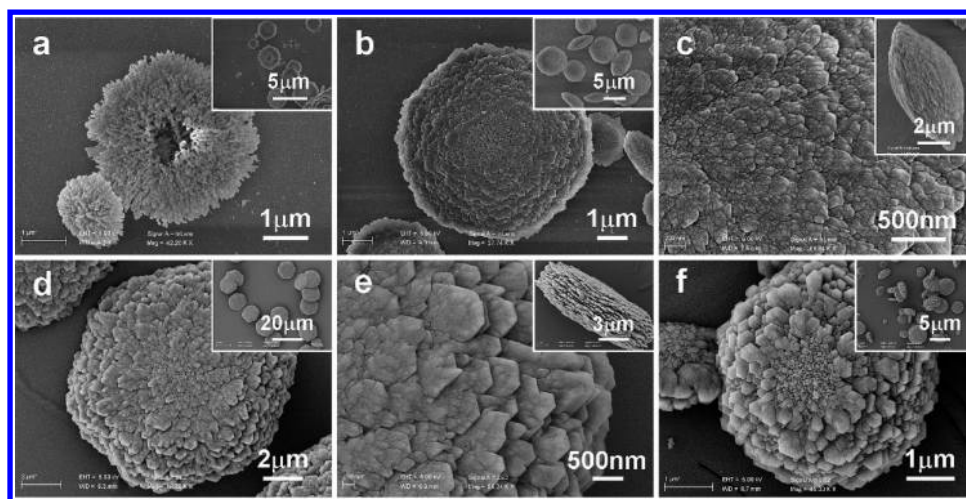


Figure 4. SEM images of vaterite aggregates and mesocrystals obtained after 24 h crystallization at $10 \pm 2^\circ\text{C}$ with different R values: 7/3 (a); 5/5 (b,c); 4/6 (d,e); 3/7 (f). The concentrations of Ca^{2+} and PSS were 1.5 mM and $0.5\text{ g}\cdot\text{L}^{-1}$, respectively.

of the morphology and assembly of the as-prepared vaterite crystals are seen at relatively low temperatures (ca. 10°C), as shown in Figure 4. Microrings with bicontinuous architecture composed of nanoparticles started to appear at $R = 7/3$ (Figure 4a). From the inset in Figure 4a, it can be seen that not all vaterite aggregates have ring-like structures, and some samples form in plate-like structures without a hole in the center of the plate (see Supporting Information, Figure S2a). However, the bicontinuous architecture is retained in these plate-like aggregates. Upon decreasing the R value of DIW/ethanol to 5/5, lens-like vaterite agglomerates are deposited with typical size of $7\text{ }\mu\text{m}$ diameter and $4\text{ }\mu\text{m}$ thickness at the center (Figure 4b,c). The surfaces of these vaterite lenses are covered by scale-like nanounits with relief substructures fused from primary nanoparticles (Figure 4c). Shao and co-workers fabricated similar structures using silk fibroin as the crystal growth modifier at 5.0 MPa and 60°C .⁵² The overall outline of vaterite lenses from top view exhibits a fuzzy, hexagonal shape, as shown in Figure 4b.

Further decreasing the R value to 4/6 produces uniform vaterite mesocrystals ($10\text{ }\mu\text{m}$ diameter) which are stacked with several smaller flake-like building blocks along the vaterite [001] direction, developing integrated multilayer superstructures (Figure 4d,e). Both the mesocrystals' profile and their basic building blocks exhibit clear hexagonal features, indicating a continual mesoscopic assembly process of hexagonal nanoflakes for the formation of the complete mesocrystals.⁵³ The relief substructures on the nanoflakes are lessened but still remain, as shown in the enlarged view (Figure 4e). The sizes of the mesocrystal rim and center are almost the same, and some of the nanoflakes exhibit obtuse edges and corners. It can be easily measured from the side-view image (inset in Figure 4e) that the thickness of vaterite nanoflakes is in the range of 100–300 nm, whereas the mesocrystals have a typical thickness of $4.3\text{ }\mu\text{m}$. Since ethanol is a bad solvent for PSS,⁵⁴ the smallest R value was 3/7 in the current study, as in our previous one,⁵¹ which results in similar multilayered mesocrystals (Figure 4f) with decreased size and increased size distribution compared with those obtained at $R = 4/6$. However, obvious variations on the morphology of its building blocks can be found. These nanounits have very smooth surfaces and angular and sharp edges and corners, as shown in Figure 4f. Besides, the thickness of the hexagonal nanoflakes decreased to the range of 50–150

nm (see Supporting Information, Figure S2b). Furthermore, the center of the multilayered mesocrystals was more porous and consisted of several irregular nanoparticles (Figure 4f). The slight difference in the size of the basic building blocks indicates different extents of fusion.⁵²

Figure 5 shows the results of TEM, HR-TEM, and SAED analyses of vaterite microrings and hexagonal mesocrystals. The

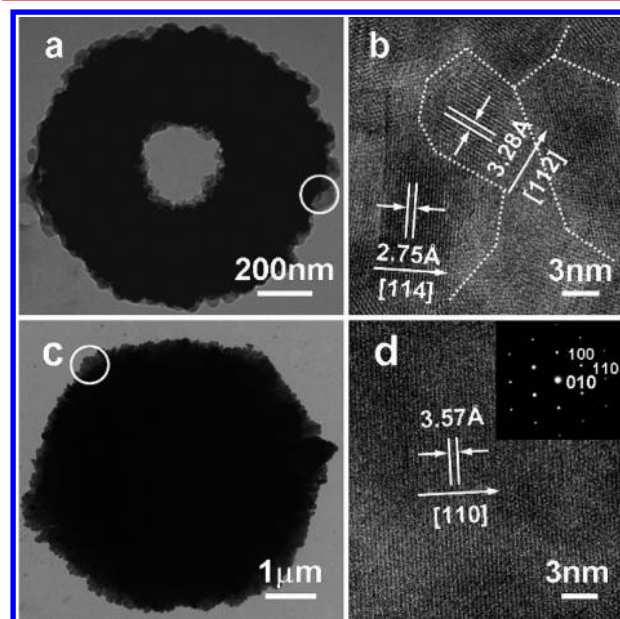


Figure 5. Representative TEM (a,c) and HR-TEM (b,d) images of vaterite microrings and mesocrystals obtained after 24 h crystallization at $10 \pm 2^\circ\text{C}$ with different R values: 7/3 (a,b); 4/6 (c,d). Dashed lines in panel (b) indicate crystalline boundaries. Inset in panel (d) corresponds to the SAED pattern taken along vaterite [001]. The concentrations of Ca^{2+} and PSS were 1.5 mM and $0.5\text{ g}\cdot\text{L}^{-1}$, respectively.

size of the primary CaCO_3 nanoparticles that agglomerate to form a vaterite microring is just several to tens of nanometers (Figure 5b). Their boundaries are indicated by dashed lines in the HR-TEM image (Figure 5b). The lattice spacings of 2.75 and $3.28\text{ }\text{\AA}$ correspond to the (114) and (112) planes of vaterite, respectively. It can also be noticed that the primary

nanoparticles arrange randomly instead of along a certain crystallographic direction. This aggregation behavior is consistent with its XRD pattern, which is a typical XRD pattern with characteristic diffraction peaks (Figure 1c). On the other hand, the vaterite mesocrystal demonstrates a mesoscopic assembly arrangement. The HR-TEM image and SAED pattern of a single nanoflake building block confirm its single-crystal nature (Figure 5d). The SAED pattern can be indexed as vaterite viewed along the [001] direction, implying that vaterite flakes expose their (001) planes, which agrees very well with its XRD pattern (Figure 1d) and SEM images (Figure 4d,e).

3.2. Crystallization of CaCO_3 Mesocrystals at 40 ± 2 °C. When the mineralization reaction was carried out at the temperature of 40 ± 2 °C, calcite was still the dominate phase of as-prepared CaCO_3 obtained at low ethanol concentrations (Figure 6a,b). However, with sustained increasing of the

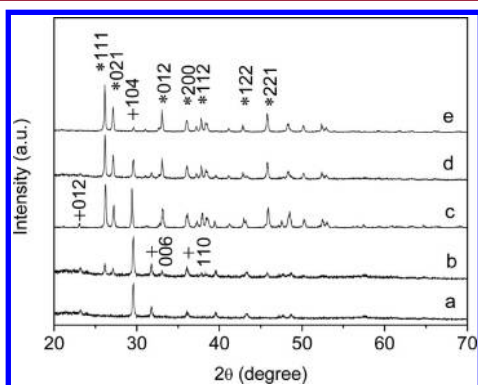


Figure 6. XRD patterns of the CaCO_3 samples obtained after 24 h crystallization at 40 ± 2 °C with different R values: 10/0 (a); 8/2 (b); 6/4 (c); 4/6 (d); 3/7 (e). The concentrations of Ca^{2+} and PSS were 1.5 mM and $0.5 \text{ g}\cdot\text{L}^{-1}$, respectively. + and * here represent peaks for calcite and aragonite, respectively.

amount of ethanol in the mixed solvent, aragonite (JCPDS card no. 41-1475) instead of vaterite started to precipitate (Figure 6b), gradually increased in quantity (Figure 6c,d), and finally became the dominant phase at higher ethanol contents (Figure 6e). Different from what happened at the low temperature of 10 ± 2 °C, there still exists a trace amount of calcite, instead of

pure aragonite, in the final CaCO_3 sample produced at $R = 3/7$, as indexed in its XRD pattern (Figure 6e).

The calcite mesocrystals obtained at 40 ± 2 °C are similar to those precipitated at 10 ± 2 °C where the initial mixed solvent has the same composition (the same R value of DIW/ethanol). The main difference is that relatively higher temperature results in calcite mesocrystals with more-developed morphologies (see Supporting Information, Figure S3). With low concentrations of ethanol, the exposure of calcite (001) faces and the multilayered structures on (104) faces is more pronounced (Figure S3a–d) compared with the samples displayed in Figure 2a,b. For those prepared at high ethanol concentrations, the platelet-like building blocks making up spherical superstructures become thinner and smaller (Figure S3e–h). From the enlarged SEM image, it can be seen that the nanoplatelets exhibit very smooth surfaces and are more compact (Figure S3h) than mesoporous, as shown in Figure 2e. The inner structure within a single rosette sphere displays a finer layered radical growth trend (Figure S3h).

As reflected in the XRD patterns (Figure 6), the aragonite polymorph started to precipitate when $R = 8/2$ at 40 ± 2 °C. Under these conditions, aragonite crystals existed in the form of separated rods with a diameter range of 140–800 nm, as measured from Figure 7a. With the decrease of R values in mixed solvents, aragonite rods with similar diameter (typically several microns) and smooth surface tend to aggregate together, parallel to their long axis direction, via an oriented attachment growth mechanism to form aragonite bundles (Figure 7b and Supporting Information, Figure S4). This oriented attachment process results in substantial elimination of the surface free energy; thus, it is a spontaneous process from the thermodynamic viewpoint. Similar bundled aggregates of aragonite rods could be produced via direct growth or dissolution–recrystallization processes under the control of regenerated silk fibroin.⁵⁵

For $R = 5/5$, these aragonite rods became more densely stacked and their fusion is upgraded, as shown from Figure 7c. While the number of these rods is increased, both their diameter and length are obviously decreased. More importantly, thinner nanoneedles protrude from corners of both terminates of a single rod, making the whole aggregate a mesoscale assembled shuttle-like superstructure, that is, aragonite

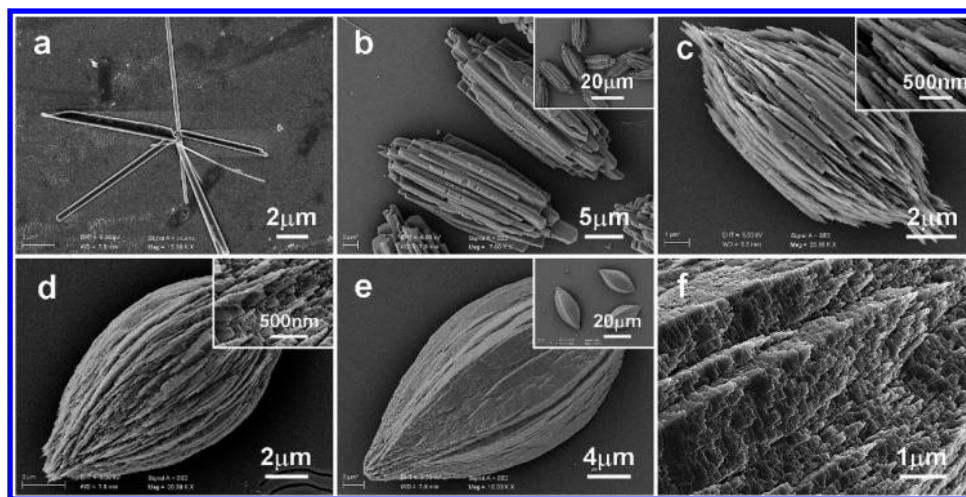


Figure 7. SEM images of aragonite rods and bundles obtained after 24 h crystallization at 40 ± 2 °C with different R values: 8/2 (a); 7/3 (b); 5/5 (c); 4/6 (d); 3/7 (e,f). The concentrations of Ca^{2+} and PSS were 1.5 mM and $0.5 \text{ g}\cdot\text{L}^{-1}$, respectively.

mesocrystals. This mineralization behavior and growth trend is further pronounced when the R value is decreased to 4/6, as illustrated in Figure 7d. It is worth noting that the lengths of the middle part of a single rod and the nanoneedle protrusions are significantly reduced compared with those obtained at $R = 5/5$ (Figure 7c). Finally, under the highest ethanol concentration ($R = 3/7$), well-developed shuttle-like aragonite mesocrystals with defined faceted surfaces are produced (Figure 7e). It is hard to separate a single aragonite rod from others because of their profound fusion. A great deal of stair-like substructures can be clearly observed on their exposed surfaces, as shown in their enlarged SEM image (Figure 7f). As we previously reported,⁵¹ the addition of ethanol into CaCl_2 aqueous solution induced a transformation from thermodynamic control to kinetic control over CaCO_3 crystallization. The size decrease and quantity increase of aragonite nanounits precisely verified this switch in turn, for ethanol facilitates the nucleation of CaCO_3 crystals.

To further investigate in depth the growth habits of aragonite rods that existed individually or assembled into shuttle-like mesocrystals, TEM, HR-TEM, and SAED analyses were carried out. A single aragonite rod displays a well-developed crystalline feature, as demonstrated by its HR-TEM image (Figure 8b)

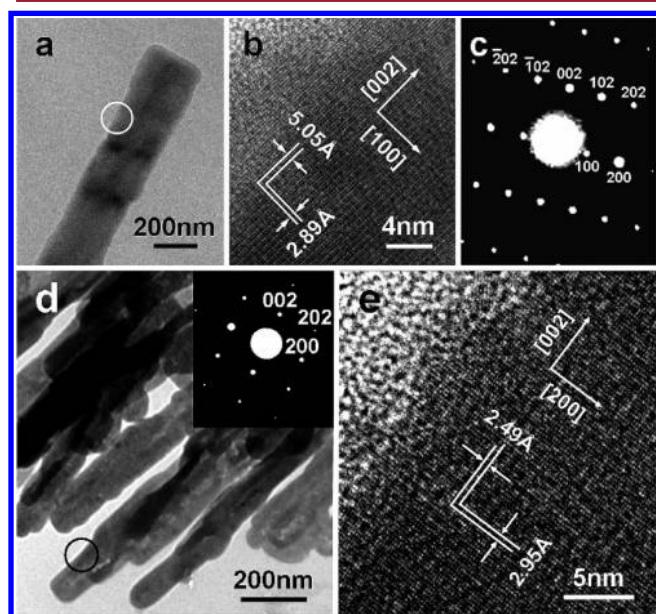


Figure 8. TEM and HR-TEM images and SAED patterns of a single aragonite rod and shuttle-like mesocrystal obtained after 24 h crystallization at 40 ± 2 °C. The R values of DIW/ethanol are 8/2 (a–c) and 4/6 (d,e). The concentrations of Ca^{2+} and PSS were 1.5 mM and $0.5 \text{ g} \cdot \text{L}^{-1}$, respectively.

and SAED pattern (Figure 8c), both of which are obtained along the $[010]$ zone axis. The clearly resolved lattice fringes of the (100) ($d = 5.05 \text{ Å}$) and (002) ($d = 2.89 \text{ Å}$) crystal faces and the sharp SAED pattern confirm the single-crystal nature of each rod and that the rod grows along the $[001]$ direction. The aragonite rods assembled into shuttle-like mesocrystals exhibit the same growth behavior as those separated ones, despite a little difference in size, as concluded from Figure 8d,e.

3.3. Polymorph Selection and Structure Evolution. PSS and PSS-containing copolymers have been widely chosen as crystal growth modifiers to mediate the crystallization of CaCO_3 , and they demonstrate extreme versatility in inducing the formation of a wide range of CaCO_3 particles with

ingenious morphologies or complex superstructures, including single crystals, mesocrystals, and polycrystalline aggregates.^{36,37,42,56–58} As mesocrystals are a new type of superstructured matter with potentially exciting applications in material construction, as exploited by nature for the formation of biominerals, they attract relatively more attention.⁵⁹ It is well known that CaCO_3 has three anhydrous polymorphs: calcite (dominant phase at lower temperatures), aragonite (dominant phase at higher temperatures), and vaterite (commonly found at higher supersaturations).^{51,60} Mesocrystals of CaCO_3 with one of the above three polymorphs have been achieved in separate systems.^{36,37,53,56,61} However, to the best of our knowledge, CaCO_3 mesocrystals with all three polymorphs bearing continuously evolved structures in one system have not been obtained by simply tuning the mineralization conditions, such as temperature and solvent composition.

Wang et al. systematically studied the growth of calcite mesocrystals in aqueous solutions by changing Ca^{2+} and PSS concentrations.^{36,37} Since the (001) faces of calcite are composed of only Ca^{2+} (Figure 9a–c), these faces are highly positively charged. Therefore, the authors proposed that the formation of calcite mesocrystals started from the preferential adsorption of negatively charged PSS molecules onto these (001) faces, which is considered a common phenomenon in several bioinspired mineralization systems,⁶² such as carbonate,^{41,63} phosphate,⁶⁴ and oxalate.⁶⁵ This preferential adsorption would induce the formation of nanosheet building blocks with exposed (001) faces and thus build up an inner dipole field along the c axis within the crystal,³⁷ as first proposed by Kniep and co-workers.⁶⁶ Finally, calcite mesocrystals were formed through the mesoscale assembly of nanosheet building blocks, driven by the above dipole effects, rather than the classical growth process of atom-by-atom addition.^{36,37} It should be pointed out that increased Ca^{2+} and PSS concentrations resulted in calcite mesocrystals with more developed structural arrangements. Subsequently, we synthesized a series of calcite mesocrystals with continuously developed morphologies by balancing the thermodynamic control and kinetic control by addition of ethanol into Ca^{2+} aqueous solutions at room temperature,⁵¹ which is similar to the present case (Figure 2 and Supporting Information, Figure S2).

In a water/ethanol binary solution system, ethanol would act as a cosurfactant at low concentration and as a cosolvent at high concentration.^{51,67} With decreasing R value, more and more ethanol molecules would enter into the solvated layer around Ca^{2+} .⁴⁷ It is well known that the interactions between Ca^{2+} ions and ethanol molecules are slightly weaker than those of Ca^{2+} ions and water molecules. Therefore, higher ethanol concentration results in easier desolvation of solvated Ca^{2+} ions, and thus favors the nucleation step of CaCO_3 crystallization to form metastable polymorphs (here, vaterite).⁴⁷ In a word, higher R values in the solvent mixture induced CaCO_3 crystallization to transform from a thermodynamically controlled process into a kinetically controlled one. This transformation changes the polymorph of as-prepared CaCO_3 from calcite to vaterite, since kinetic conditions usually induce and stabilize CaCO_3 crystals in the phase of vaterite.^{44,51} This switch can be further confirmed by the increased number and decreased size of the nanoscale primary building units from which the obtained mesocrystals are fabricated, as shown in Figures 2 and 4. Meanwhile, alcohols themselves can facilitate the precipitation

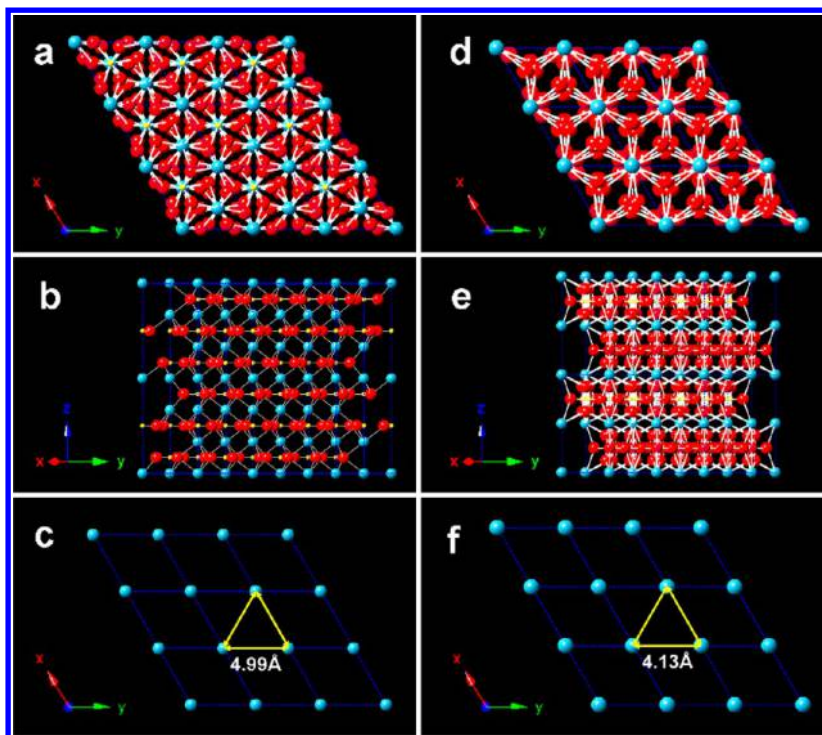


Figure 9. Crystal structures of different CaCO_3 polymorphs. (a–c) Top and side views of calcite (001) plane ($3 \times 3 \times 1$); (d–f) top and side views of vaterite (001) plane ($3 \times 3 \times 2$). (c,f) A single layer of (001) plane composed of only Ca^{2+} for calcite and vaterite, respectively. Blue, Ca; yellow, C; red, O.

rate of vaterite and stabilize CaCO_3 in the form of vaterite by preventing its subsequent transformation into calcite.^{47,60}

What is more, the phase change from calcite to vaterite and the formation of vaterite mesocrystals at low temperature could also be explained by the transitions of the molecular conformation of PSS with increased ethanol content and its preferential adsorption on (001) faces of both calcite and vaterite (Figure 9). In water system, the backbone of the PSS molecule is fully stretched because the negatively charged units repel each other, as shown in the top panel of Figure 10a.⁶⁸

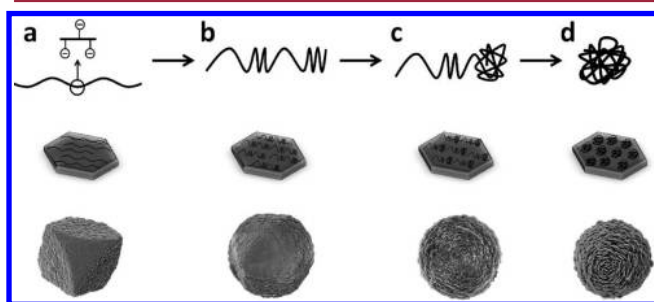


Figure 10. Schematic presentations of the molecular conformation of PSS (top panels) and absorption of PSS molecules on calcite (001) faces (middle panels), and corresponding typical calcite mesocrystals (bottom panels) with different ethanol contents in solutions. The ethanol content is continuously increased from (a) to (d).

Under these conditions, PSS molecules preferentially bind to the polar calcite (001) face (Figure 9c) by both direct and solvent-mediated binding, leading to the formation of calcite mesocrystals, which has been proved by molecular dynamics simulations at the molecular level very recently.⁶⁹ However, with the ethanol fraction increasing, PSS molecules tend to fold and self-cross, exhibiting a coil or even globule conformation

with many kinks (Figure 10b–d, top panels).⁶⁸ This conformational transition makes it match with the vaterite (001) face properly, since the distance between two neighboring Ca atoms of the vaterite (001) face (4.13 \AA) is smaller than that in calcite (4.99 \AA) (Figure 9c,f), making the metastable polymorph vaterite more stable than calcite.⁶⁰

In addition to stabilizing the vaterite phase, the conformational change of PSS molecules also plays an important role in the development of calcite and vaterite mesocrystals through particle-based assembly. With fully stretched conformation in water, PSS molecules will selectively absorb on calcite (001) crystal faces (Figure 10a, middle panel) and reduce their growth rate.^{36,37,51} However, since the concentration of PSS is relatively lower, the influence imposed by PSS is weaker (Figure 10a, bottom panel) than in our previous studies.⁵¹ With increasing ethanol content in mixed solvents, the folded and self-crossed conformation of PSS molecules becomes more and more prominent (Figure 10b–d, top panels).⁶⁸ It is intuitively clear that this structural change will certainly reduce the size of PSS molecules, and thus result in an increased number of adsorbed PSS molecules on CaCO_3 nanoplates (Figure 10b–d, middle panels). Therefore, the dipole field between two adjacent CaCO_3 nanoplates becomes stronger and stronger, leading to continuously increasing distance between these two adjacent nanoplates, and finally the increasingly developed mesocrystal structures (Figure 10b–d, bottom panels). This development trend could also be observed in Wang's system, where they realized it via increasing the PSS concentration.³⁷ In addition, folded or self-crossed PSS molecules are not sufficient to stabilize the primary vaterite nanoparticles; instead, they could stabilize larger hexagonal plate-like building blocks and arrange them into ordered mesocrystals (Figure 4d–f).⁵³

It is very important and worth noting that a slightly higher temperature ($40 \pm 2 \text{ }^\circ\text{C}$) could cause dramatic variations in the

CaCO_3 polymorph (Figure 6) and its structural arrangement (Figure 7). Whereas the polymorph of CaCO_3 was primarily determined by R values and the resulting conformational change of PSS molecules at a lower temperature of $10 \pm 2^\circ\text{C}$, temperature effects became more obvious in controlling the CaCO_3 polymorph at $40 \pm 2^\circ\text{C}$, which can be explained from the viewpoint of energy. According to Gibbs's theory,⁷⁰ two main parts, bulk lattice energy (ΔG_b) and surface energy (ΔG_s), combine to constitute the total energy of a crystal (ΔG). Previously, De Leeuw and Parker reported that the three anhydrous polymorphs of CaCO_3 exhibited quite similar lattice energies: calcite, $-1.6867 \times 10^8 \text{ kJ}\cdot\text{mol}^{-3}$; aragonite, $-1.7851 \times 10^8 \text{ kJ}\cdot\text{mol}^{-3}$; vaterite, $-1.6577 \times 10^8 \text{ kJ}\cdot\text{mol}^{-3}$. However, their surface energies are far different, increasing following the order of calcite–vaterite–aragonite with a ratio of 1:1.6:2.⁷¹ Meanwhile, the solvent nature can directly influence the surface energies of all three polymorphs, and thus the total energy and resulting polymorph.⁵⁰ This influence may be another reason why vaterite can be prepared with high solvent ethanol content at $10 \pm 2^\circ\text{C}$. However, temperature effects dominate at $40 \pm 2^\circ\text{C}$. Therefore, as we previously reported, higher temperature facilitates the formation of the phase with higher total energy;³⁹ thus, the precipitated CaCO_3 at $40 \pm 2^\circ\text{C}$ existed in the aragonite phase. Aragonite is precipitated at higher temperatures, an effect that can also be explained by kinetic control, due to higher growth rates of aragonite as compared to the other polymorphs.⁶⁰ Although it can be clearly found that there is no lattice match between PSS molecules and aragonite crystals (exposed (010) face shown in Supporting Information, Figure S4), the aragonite phase can also be produced under the favor of energy mediation and kinetic controls induced by ethanol fraction increase and higher temperature.

4. CONCLUSION

In summary, it has been demonstrated that CaCO_3 mesocrystals of all three polymorphs can be selectively produced in one mineralization system in the presence of PSS simply by adjusting the aqueous phase volume ratio (R value) of DIW/ethanol and the reaction temperature. These mesocrystals exhibited continuously evolving superstructures, with their nanoscale building blocks assembling into ordered arrangements with decreasing R value in the solvent mixture. At a relatively lower reaction temperature (10°C), the main effect over CaCO_3 crystallization was imposed by the R value of DIW/ethanol and the resulting conformational change of the PSS molecules, which resulted in a polymorph change of CaCO_3 crystals from pure calcite to pure vaterite. The structural development of calcite and vaterite mesocrystals was proposed to be directly related to the dipole effects established between neighboring PSS-adsorbed nanosheet building units. In contrast, at a relatively higher reaction temperature (40°C), the temperature effect became more obvious and the dominant one in controlling the polymorph and structural arrangement of deposited CaCO_3 crystals. As the R value decreased, the phases of precipitated CaCO_3 crystals changed from pure calcite to almost pure aragonite. This study provides definite evidence of the importance of the synergetic effects derived from mixed solvent and temperature in controlling the polymorph and mesoscopic assembly of inorganic crystals. Meanwhile, the successful realization of polymorph selection and mesocrystals with consecutively evolved morphologies in the present case could provide a deeper understanding for some CaCO_3 -related biomineraliza-

tion processes, such as those in mollusk shells, where calcite and aragonite can be selectively produced with special and uniform morphologies and arrangement in different positions under similar external conditions. In addition, these mesocrystals may further act as precursors or templates to prepare other materials with mesoporous structures and ordered arrangement.

■ ASSOCIATED CONTENT

Supporting Information

Experimental apparatus, SEM images, and crystal structure of aragonite. This material is available free of charge via the Internet at <http://pubs.acs.org>.

■ AUTHOR INFORMATION

Corresponding Author

*Fax: +86 551 63603040. E-mail: shyu@ustc.edu.cn.

Notes

The authors declare no competing financial interest.

■ ACKNOWLEDGMENTS

We acknowledge the special funding support from the Ministry of Science and Technology of China, the National Basic Research Program of China (Grants 2010CB934700, 2013CB933900, 2014CB931800), the National Natural Science Foundation of China (Grants 21431006, 91022032, 91227103), the Chinese Academy of Sciences (KJZD-EW-M01-1), the China Postdoctoral Science Foundation (BH2060190050), and the Fundamental Research Funds for the Central Universities (WK2060190034).

■ REFERENCES

- (1) Mayer, G. *Science* **2005**, *310*, 1144–1147.
- (2) Meyers, M. A.; McKittrick, J.; Chen, P. Y. *Science* **2013**, *339*, 773–779.
- (3) Aizenberg, J.; Weaver, J. C.; Thanawala, M. S.; Sundar, V. C.; Morse, D. E.; Fratzl, P. *Science* **2005**, *309*, 275–278.
- (4) Addadi, L.; Weiner, S. *Nature* **1997**, *389*, 912–914.
- (5) Kirschvink, J. L. *Nature* **1997**, *390*, 339–340.
- (6) Aizenberg, J.; Tkachenko, A.; Weiner, S.; Addadi, L.; Hendler, G. *Nature* **2001**, *412*, 819–822.
- (7) Nudelman, F.; Chen, H. H.; Goldberg, H. A.; Weiner, S.; Addadi, L. *Faraday Discuss.* **2007**, *136*, 9–25.
- (8) Meldrum, F. C.; Cölfen, H. *Chem. Rev.* **2008**, *108*, 4332–4432.
- (9) Chen, S. F.; Zhu, J. H.; Jiang, J.; Cai, G. B.; Yu, S. H. *Adv. Mater.* **2010**, *22*, 540–545.
- (10) Nudelman, F.; Sommerdijk, N. A. J. M. *Angew. Chem., Int. Ed.* **2012**, *51*, 6582–6596.
- (11) Meldrum, F. C. *Int. Mater. Rev.* **2003**, *48*, 187–224.
- (12) Dalas, E.; Klepetsanis, P.; Koutsoukos, P. G. *Langmuir* **1999**, *15*, 8322–8327.
- (13) Sui, C.; Lu, Y.; Gao, H. L.; Dong, L.; Zhao, Y.; Ouali, L.; Benczedi, D.; Jerri, H.; Yu, S. H. *Cryst. Growth Des.* **2013**, *13*, 3201–3207.
- (14) Zhao, Y.; Lin, L. N.; Lu, Y.; Chen, S. F.; Dong, L.; Yu, S. H. *Adv. Mater.* **2010**, *22*, 5255–5259.
- (15) Zhao, Y.; Lin, L. N.; Lu, Y.; Gao, H. L.; Chen, S. F.; Yang, P.; Yu, S. H. *Adv. Healthcare Mater.* **2012**, *1*, 327–331.
- (16) Zhao, Y.; Lu, Y.; Hu, Y.; Li, J. P.; Dong, L.; Lin, L. N.; Yu, S. H. *Small* **2010**, *6*, 2436–2442.
- (17) Begum, G.; Rana, R. K. *Chem. Commun.* **2012**, *48*, 8216–8218.
- (18) Bassett, D. C.; Marelli, B.; Nazhat, S. N.; Barralet, J. E. *Adv. Funct. Mater.* **2012**, *22*, 3460–3469.

- (19) Natalio, F.; Corrales, T. P.; Panthöfer, M.; Schollmeyer, D.; Lieberwirth, I.; Müller, W. E. G.; Kappl, M.; Butt, H.-J.; Tremel, W. *Science* **2013**, 339, 1298–1302.
- (20) Gao, Y. X.; Yu, S. H.; Cong, H. P.; Jiang, J.; Xu, A. W.; Dong, W. F.; Cölfen, H. *J. Phys. Chem. B* **2006**, 110, 6432–6436.
- (21) Guo, X.; Liu, L.; Wang, W.; Zhang, J.; Wang, Y.; Yu, S. H. *CrystEngComm* **2011**, 13, 2054–2061.
- (22) Chevalier, N. R.; Chevillard, C.; Goldmann, M.; Brezesinski, G.; Guenoun, P. *Cryst. Growth Des.* **2012**, 12, 2299–2305.
- (23) Liu, L.; Hu, B.; Chen, S. F.; Liu, S. J.; Jiang, J.; Cai, G. B.; Yu, S. H. *CrystEngComm* **2010**, 12, 3593–3598.
- (24) Takiguchi, M.; Igarashi, K.; Azuma, M.; Ooshima, H. *Cryst. Growth Des.* **2006**, 6, 2754–2757.
- (25) Li, C.; Qi, L. M. *Angew. Chem., Int. Ed.* **2008**, 47, 2388–2393.
- (26) Hetherington, N. B. J.; Kulak, A. N.; Kim, Y. Y.; Noel, E. H.; Snoswell, D.; Butler, M.; Meldrum, F. C. *Adv. Funct. Mater.* **2011**, 21, 948–954.
- (27) Finnemore, A. S.; Scherer, M. R. J.; Langford, R.; Mahajan, S.; Ludwigs, S.; Meldrum, F. C.; Steiner, U. *Adv. Mater.* **2009**, 21, 3928–3932.
- (28) Liu, L.; He, D.; Wang, G. S.; Yu, S. H. *Langmuir* **2011**, 27, 7199–7206.
- (29) Chen, S. F.; Yu, S. H.; Wang, T. X.; Jiang, J.; Cölfen, H.; Hu, B.; Yu, B. *Adv. Mater.* **2005**, 17, 1461–1465.
- (30) Guo, X. H.; Yu, S. H.; Cai, G. B. *Angew. Chem., Int. Ed.* **2006**, 45, 3977–3981.
- (31) Olszta, M. J.; Gajjeraman, S.; Kaufman, M.; Gower, L. B. *Chem. Mater.* **2004**, 16, 2355–2362.
- (32) Zhu, J. H.; Song, J. M.; Yu, S. H.; Zhang, W. Q.; Shi, J. X. *CrystEngComm* **2009**, 11, 539–541.
- (33) Kato, T. *Adv. Mater.* **2000**, 12, 1543–1546.
- (34) Wei, H.; Ma, N.; Shi, F.; Wang, Z. Q.; Zhang, X. *Chem. Mater.* **2007**, 19, 1974–1978.
- (35) Finnemore, A.; Cunha, P.; Shean, T.; Vignolini, S.; Guldin, S.; Oyen, M.; Steiner, U. *Nat. Commun.* **2012**, 3, 966.
- (36) Wang, T. X.; Cölfen, H.; Antonietti, M. *J. Am. Chem. Soc.* **2005**, 127, 3246–3247.
- (37) Wang, T. X.; Antonietti, M.; Cölfen, H. *Chem.—Eur. J.* **2006**, 12, 5722–5730.
- (38) Park, R. J.; Meldrum, F. C. *Adv. Mater.* **2002**, 14, 1167–1169.
- (39) Jiang, J.; Chen, S. F.; Liu, L.; Yao, H. B.; Qiu, Y. H.; Gao, M. R.; Yu, S. H. *Chem. Commun.* **2009**, 5853–5855.
- (40) Guo, X. H.; Xu, A. W.; Yu, S. H. *Cryst. Growth Des.* **2008**, 8, 1233–1242.
- (41) Gao, Y. X.; Yu, S. H.; Guo, X. H. *Langmuir* **2006**, 22, 6125–6129.
- (42) Xu, A. W.; Dong, W.-F.; Antonietti, M.; Cölfen, H. *Adv. Funct. Mater.* **2008**, 18, 1307–1313.
- (43) Wang, T.; Porter, D.; Shao, Z. Z. *Adv. Funct. Mater.* **2012**, 22, 435–441.
- (44) Dickison, S. R.; McGrath, K. M. *J. Mater. Chem.* **2003**, 13, 928–933.
- (45) Loges, N.; Graf, K.; Nasdala, L.; Tremel, W. *Langmuir* **2006**, 22, 3073–3080.
- (46) Andreassen, J. P. *J. Cryst. Growth* **2005**, 274, 256–264.
- (47) Zhang, L.; Yue, L. H.; Wang, F.; Wang, Q. *J. Phys. Chem. B* **2008**, 112, 10668–10674.
- (48) Duan, X.; Ma, J.; Lian, J.; Kim, T.; Zheng, W. *Chem. Commun.* **2010**, 46, 7133–7135.
- (49) Guo, X. H.; Meng, F.; Qu, X.; Wang, M.; Mao, C.; Zhang, J.; Wang, W.; Yu, S. H. *CrystEngComm* **2012**, 14, 3213–3219.
- (50) Chen, S. F.; Yu, S. H.; Jiang, J.; Li, F. Q.; Liu, Y. K. *Chem. Mater.* **2006**, 18, 115–122.
- (51) Geng, X.; Liu, L.; Jiang, J.; Yu, S. H. *Cryst. Growth Des.* **2010**, 10, 3448–3453.
- (52) Wang, T.; Che, R. C.; Li, W. T.; Mi, R. X.; Shao, Z. Z. *Cryst. Growth Des.* **2011**, 11, 2164–2171.
- (53) Xu, A. W.; Antonietti, M.; Cölfen, H.; Fang, Y. P. *Adv. Funct. Mater.* **2006**, 16, 903–908.
- (54) Bakandritsos, A.; Bouropoulos, N.; Zboril, R.; Iliopoulos, K.; Boukos, N.; Chatzikyriakos, G.; Couris, S. *Adv. Funct. Mater.* **2008**, 18, 1694–1706.
- (55) Wang, T.; Porter, D.; Shao, Z. Z. *Adv. Funct. Mater.* **2012**, 22, 435–441.
- (56) Page, M. G.; Cölfen, H. *Cryst. Growth Des.* **2006**, 6, 1915–1920.
- (57) Kulak, A. N.; Iddon, P.; Li, Y.; Armes, S. P.; Cölfen, H.; Paris, O.; Wilson, R. M.; Meldrum, F. C. *J. Am. Chem. Soc.* **2007**, 129, 3729–3736.
- (58) Song, R.-Q.; Cölfen, H.; Xu, A.-W.; Hartmann, J.; Antonietti, M. *ACS Nano* **2009**, 3, 1966–1978.
- (59) Cölfen, H.; Antonietti, M. *Angew. Chem., Int. Ed.* **2005**, 44, 5576–5591.
- (60) Flaten, E. M.; Seiersten, M.; Andreassen, J. P. *J. Cryst. Growth* **2009**, 311, 3533–3538.
- (61) Zhou, G. T.; Yao, Q. Z.; Ni, J.; Jin, G. *Am. Mineral.* **2009**, 94, 293–302.
- (62) Cölfen, H.; Yu, S. H. *MRS Bull.* **2005**, 30, 727–735.
- (63) Yu, S. H.; Cölfen, H.; Tauer, K.; Antonietti, M. *Nat. Mater.* **2005**, 4, 51–55.
- (64) Jiang, H. D.; Liu, X. Y.; Zhang, G.; Li, Y. *J. Biol. Chem.* **2005**, 280, 42061–42066.
- (65) Farmanesh, S.; Ramamoorthy, S.; Chung, J.; Asplin, J. R.; Karande, P.; Rimer, J. D. *J. Am. Chem. Soc.* **2014**, 136, 367–376.
- (66) Busch, S.; Dolhaine, H.; DuChesne, A.; Heinz, S.; Hochrein, O.; Laeri, F.; Podebrad, O.; Vietze, U.; Weiland, T.; Kniep, R. *Eur. J. Inorg. Chem.* **1999**, 1643–1653.
- (67) Gharibi, H.; Razavizadeh, B. M.; Rafati, A. A. *Colloids Surf., A* **1998**, 136, 123–132.
- (68) Severin, N.; Okhapkin, I. M.; Khokhlov, A. R.; Rabe, J. P. *Nano Lett.* **2006**, 6, 1018–1022.
- (69) Shen, J. W.; Li, C.; van der Vegt, N. F. A.; Peter, C. *J. Phys. Chem. C* **2013**, 117, 6904–6913.
- (70) Gibbs, J. W. *Collected Works*; Longman: New York, 1928.
- (71) De Leeuw, N. H.; Parker, S. C. *J. Phys. Chem. B* **1998**, 102, 2914–2922.